Optoelectronic Enhancement of Ultrathin CuIn$_{1-x}$Ga$_x$Se$_2$ Solar Cells by Nanophotonic Contacts

Guanchao Yin, Mark W. Knight, Marie-Claire van Lare, Maria Magdalena Solà Garcia, Albert Polman, and Martina Schmid*

CuIn$_{1-x}$Ga$_x$Se$_2$ (CIGSe) solar cells have achieved record efficiency values as high as 22.6% for small areas, with module efficiency values of 16.5%. However, for economic viability these values must be achieved with reduced material consumption (especially indium), which requires reducing the CIGSe absorber thickness from 2000–3000 nm to below 500 nm. Soft-imprinted SiO$_x$ nanoparticles (NPs) beneath a conformal CIGSe layer enable this thickness reduction. Optically, they enhance the absorption of light through Fabry–Pérot and waveguided resonances within the CIGSe layer, preventing current loss. For CIGSe solar cells on ITO with an absorber thickness of only 390 nm and a nanophotonic contact the current density (J_{sc}) increases from 25.7 to 32.1 mA cm^{-2}. At the same time, the nanopatterned contact reduces the back barrier, leading to an increased open-circuit voltage (518 to 558 mV) and fill factor (50.7% to 55.2%). Combined, these effects increase the efficiency value from 6.8% to 10.0% for this initial demonstration. With the addition of an antireflection coating, the champion NP-enhanced cell achieves a J_{sc} of 34.0 mA cm^{-2}, corresponding to 93% of the J_{sc} achieved by the thick world-record cell. This result shows that optoelectronic nanopatterning provides a path to high efficiency cells with reduced materials consumption.

1. Introduction

CuIn$_{1-x}$Ga$_x$Se$_2$ (CIGSe) solar cells have achieved record light-to-power conversion efficiency values as high as 22.6% for small areas,[1] with 16.5% reached for module production.[2] Compared with other competing PV technologies, CIGSe solar cells offer a remarkably short energy payback time,

minimal consumption of high purity materials, high performance over a wide range of illumination intensities, and a reduced sensitivity to shading compared to Si.[3] These features make CIGSe solar cells unique in the competition to surpass crystalline Si, which currently dominates photovoltaic installations with >90% market share. Despite rapid advances in CIGSe technology, leading to performance gains of ≈0.2% absolute per year in recent years,[4] additional reductions in manufacturing cost are essential for driving large-scale deployment. Thinning the CIGSe absorber significantly below the typical 2–3 μm can enable a significant reduction in material consumption and reduce the equipment time required to deposit the absorber, thereby simultaneously addressing concerns over indium scarcity[5,6] and lowering manufacturing cost in mass production.

Presently, ultrathin CIGSe solar cells (defined as having a sub-500 nm absorber thickness) have not yet attained high efficiency values as a result of two primary challenges: recombination at the back contact, and incomplete absorption.[7–10] The problem of back recombination is particularly severe for ultrathin CIGSe solar cells where the absorber thickness (and rear contact) is within the diffusion length of carriers. The back recombination can be addressed by adding a Ga grading, which creates a potential for electrons through an increasing [Ga]/[[Ga]+[In]] ratio toward the back contact,[8,10] and by using rear-surface point contacts to reduce the interface recombination velocity.[11] Incomplete optical absorption is the second major challenge for ultrathin CIGSe solar cells and leads to a reduced a short-circuit current density (J_{sc}). Ultrathin cells typically show a J_{sc} below 30 mA cm^{-2}, a loss of more than 6 mA cm^{-2} compared to thick cells.[7–9] Due to the poor optical reflectivity of Mo–MoSe$_2$, a significant fraction (>80%) of the light reaching the rear interface is absorbed rather than being reflected back into the CIGSe absorber layer.[12] This parasitic absorption in Mo (Abs$_{Mo}$) is a key source of optical loss. Prior work has shown modest J_{sc} gains via texturing the front surface, and by replacing the typical CdS buffer layer by a higher bandgap Zn(O,S).[7] However, these schemes failed to substantially reduce Abs$_{Mo}$ as the J_{sc} increase was limited to the optical path-length

Dr. G. Yin, Prof. M. Schmid
Nanooptische Konzepte für die PV
Helmholtz-Zentrum Berlin für Materialien und Energie
Hahn-Meitner-Platz 1, 14109 Berlin, Germany
E-mail: martina.schmid@helmholtz-berlin.de
Dr. M. W. Knight, Dr. M.-C. van Lare,
M. M. Solà Garcia, Prof. A. Polman
Center for Nanophotonics
FOM Institute AMOLF
Science Park 104, 1098 XG, Amsterdam, The Netherlands
Prof. M. Schmid
Department of Physics
Freie Universität Berlin
Arnimallee 14, 14195 Berlin, Germany

enhancement obtained for a single-pass. In another approach the poor CIGSe/Mo interface reflectivity was addressed by transferring cells from Mo onto Au, giving a pronounced absorption enhancement in the CIGSe layer.[13] However, this approach is limited to transferred areas of only a few cm², and the near-bandgap enhancement was weak since only a double-pass optical enhancement was attained.

Metallic nanoparticles (NPs) have been proposed as a tool for achieving enhanced light absorption in photovoltaic applications due to their plasmonic resonances, which give rise to strong scattering and enhanced near fields.[14–16] However, plasmonic particles suffer from intrinsic parasitic absorption which constrains their potential for achieving optical enhancements in solar cells with an already-high EQE.[17] The potential for plasmonic nanoparticles on CIGSe is compounded by instability; the least lossy plasmonic materials (Au, Ag) degrade and can diffuse at the (relatively high, >400 °C) temperatures used for cell fabrication.[18]

In recent years, wavelength-scale dielectric NPs, which show equally high scattering cross sections as metallic NPs but are free of absorption,[19] have been proposed as efficient scatterers.[20,21] Unlike metals, inorganic dielectrics (e.g., SiO_2 and Al_2O_3) exhibit excellent thermal stability which is essential for integration with CIGSe cells. Some dielectric materials also contain an intrinsic charge, which was proved to electrically benefit solar cells.[11,22] These unique features suggest that dielectric nanoparticles are a promising option for improving absorption in ultrathin CIGSe solar cells.

In our previous work, we placed SiO_x nanoparticles at the rear interface of CIGSe/Mo and achieved absorption enhancement within the CIGSe by reducing Abs_{Mo}.[23] While significant enhancements resulted from scattering by the nanoparticles, some light still reached the Mo back contact and resulted in residual parasitic Abs_{Mo}. This occurred even for optimized nanopatterns, indicating that ultrathin CIGSe solar cells on Mo are unlikely to reach or exceed the J_{sc} of their standard thick counterparts. An alternative approach is to prepare CIGSe cells on a transparent conductive oxide (TCO),[24–26] such as ITO (Sn:In₂O₃) or FTO (F:SnO₂), which can significantly reduce parasitic absorption compared to Mo. Light trapping nanostructures enable near-complete absorption for above-bandgap photons, significantly exceeding the double-pass absorption for planar devices, while reducing parasitic optical loss in the below-bandgap regime. This is of particular interest in emerging multijunction and bifacial devices.[27] Alternatively, transmitted light can then be returned to the cell with extremely high efficiency values using a lossless reflector at the rear side of the glass substrate.

In this contribution we demonstrate large-area SiO_x nanoparticle arrays embedded at the rear interface of ultrathin CIGSe solar cells grown on ITO. Nanostructuring is shown to reduce the potential barrier at CIGSe/ITO interface (back barrier) of the cells, while simultaneously yielding a significant 5.0 mA cm⁻² increase in J_{sc} for ultrathin CIGSe solar cells with an absorber thickness of only 390 nm. When applied in conjunction with a rear reflector and an antireflection coating, our champion cell achieves a J_{sc} of 34.0 mA cm⁻² which is, to date, the highest experimental J_{sc} reported for any ultrathin CIGSe solar cell.

2. Results and Discussion

2.1. Fabrication and Modeling of CIGSe Cells on Nanophotonic Contacts

Substrate conformal imprint lithography (SCIL)[28] was employed to fabricate the dielectric SiO_x nanoparticles in this work. The SCIL approach combines rapid and high fidelity wafer-scale replication of nanoparticle arrays, tolerance of substrate defects, and room temperature atmospheric processing.[29] A detailed description of the nanophotonic contact preparation is available in the Experimental Section: Fabrication of SiO_x Nanoparticles on ITO Substrates.
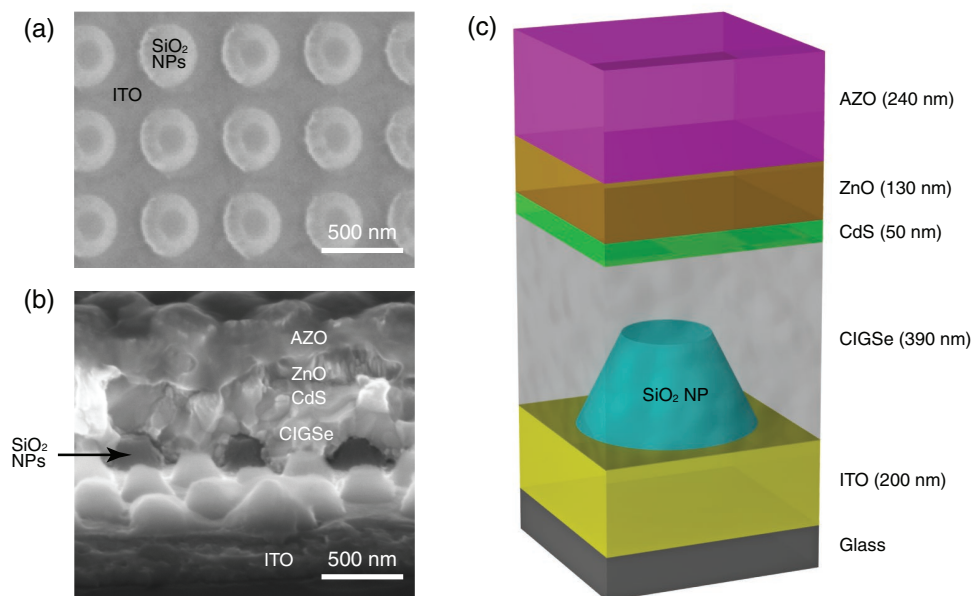
Figure 1a shows the scanning electron microscope (SEM) image of SiO_x nanostructures on ITO substrate, which were completely isolated and arranged in a tetragonal array with a pitch of 513 nm. Within this array, the individual nanoparticles were closely approximated as conical frustra; simulations assumed a homogeneous array of NPs that were 210 nm high with base and top diameters of 205 and 102 nm, respectively (Figure 1c). The structure of a fabricated ultrathin CIGSe solar cell is shown in Figure 1b, indicating the layers of ZnO:Al(AZO)/i-ZnO/CdS/CIGSe/ITO/glass substrate from top to bottom. The absorber is only 390 nm thick with a [Ga]/([Ga]+[In]) of 0.36 and [Cu]/([Ga]+[In]) of 0.87. These ratios match those used in record-class CIGSe cells, and were selected to both optimize cell efficiency and enable a direct comparison with previous cell designs using thicker absorber layers. A detailed description of cell preparation is available in the Experimental Section: Preparation Details of CIGSe Solar Cells.

The conformal coating of the nanopatterned electrode satisfies the geometrical requirement for a good electrical contact. Importantly, the SiO_x nanoparticles reduce the contacting area between the CIGSe layer and ITO without hindering carrier collection, because the maximum path of carriers to pass beside a single SiO_x NP is within the diffusion length of minority carriers (0.5–1 μm) for CIGSe solar cells.[11]

To study the light trapping effects of SiO_x nanoparticle arrays in detail, periodic 3D finite-difference time-domain (FDTD) simulations were carried out using single-frequency calculations (see the Experimental Section: FDTD Modeling). This approach allowed the model to use measured dielectric functions for all materials (SiO_x, ITO, CIGSe, CdS, ZnO, AZO) at each frequency without error-prone broadband modeling of their complex dielectric functions. The optical constants for the thin film layers comprising the cell were extracted based on transmission and reflection measurements via transfer-matrix method;[30] tabulated literature values were used for the SiO_x and Ag dielectric functions.[31] The unit cell simulated in FDTD is shown in Figure 1c, with the layer thicknesses specified according to measured thicknesses from the fabricated cells. For all cells (flat and with nanopatterning) the total CIGSe absorber volume was held constant at (513 nm)² × 390 nm.

2.2. External Quantum Efficiency Spectra

The measured external quantum efficiency (EQE) and reflection/transmission (R/T) curves for bare and SiO_x

**ADVANCED
SCIENCE NEWS**
www.advancedsciencenews.com

**ADVANCED
OPTICAL
MATERIALS**
www.advopticalmat.de

FULL PAPER

Figure 1. Fabricated and modeled cell geometry. a) Top view SEM image of SiO_x nanostructures on ITO prior to CIGSe deposition and b) cross section of the complete ultrathin CIGSe solar cell with SiO_x nanoparticles at the rear CIGSe/ITO interface. c) Illustration of the ultrathin CIGSe solar cell geometry as modeled in FDTD simulations. Based on the measured dimensions of as-fabricated NPs, the modeled SiO_x particle was a conical frustrum with dimensions of (r_{base}, r_{top}) = (205, 102) nm, with a height of 210 nm. The unit cells of the square array had pitch of 513 nm.

nanopatterned cells are compared in **Figure 2**a,b. The bare cell (black) reaches a maximum EQE of 80% at 550 nm, which is limited by front-surface reflection. For longer wavelengths, incomplete absorption in the ultrathin CIGSe layer leads to a drop in EQE with a corresponding increase in T. After incorporating SiO_x nanoparticles (red), the EQE significantly increases from 550 to 1200 nm, with a concomitant decrease in T, yielding a total AM1.5-integrated J_{sc} enhancement of 5.2 mA cm^{-2} (25.7 to 30.9 mA cm^{-2}).

Unlike optically lossy Mo, the ITO contact permits use of a mirror at the rear side of the glass substrate (Figure 2a, green line). With the addition of a 200 nm Ag rear reflector a significant EQE enhancement results for wavelengths in the 550–1150 nm range, further boosting the integrated J_{sc} to 32.1 mA cm^{-2}. Since the Ag reflector is not integrated within the CIGSe structure, comparable back reflection (and corresponding performance enhancements) could also be achieved using either Al or dielectric scatterers on the back of the glass substrate.[32]

To confirm that the measured EQE enhancements were due to optical modification by the SiO_x nanoparticles, both Abs_{CIGSe}/Abs_{ITO} and R/T were modeled using FDTD (Figure 2c,d). The simulated Abs_{CIGSe} curves for bare and nanopatterned cells agree well with the experimentally measured EQE curves, with all of the major spectral features reproduced in both wavelength and amplitude. The close agreement of these curves shows that the FDTD model is capturing the essential optical properties of the ultrathin cells. This also suggests that the losses in internal quantum efficiency (IQE), shown in Figure S2 of the Supporting Information, can be attributed primarily to parasitic absorption within the front-surface layers and the rear ITO, as the losses in IQE significantly exceed the discrepancy between the modeled CIGSe absorption and measured EQE curves. This

implies that photons absorbed within the CIGSe layer have a high (near unity) probability of charge collection.

The minor discrepancies between the measurements and model arise from differences in the assumed geometry. For the nanoparticle-enhanced cells (red), there is an additional measured enhancement beyond that predicted by the model. This is attributed to an antireflection effect (Figure 2b,d; R) caused by the conformal growth process, which produces front surface texturing and is absent in the modeled geometry. Conversely, for the cell with both SiO_x nanoparticles and rear reflector, the modeled EQE enhancement is higher than the measured enhancement. The reason for this discrepancy is twofold: first, parasitic absorption in the experimental soda lime glass substrate is not considered in the simulation and second, the experimental Ag film likely exhibited a lower reflectivity than the smooth Ag mirror used in the model due to local symmetry breaking by surface roughness, creating localized lossy resonances capable of coupling with the dipolar field of light.

The FDTD model also allows the identification of optical loss mechanisms within the cell which could not be directly measured, including absorption by the ITO. Parasitic ITO absorption is found to be an important parasitic loss channel (Figure 2c, dashed lines). The magnitude of the absorption by the ITO corresponds to the high electrical conductivity (<10 Ω sq^{-1}) required for the cell design used in this work. Interestingly, the parasitic ITO absorption slightly decreases with the addition of the SiO_x nanoparticles as the CIGSe absorption is enhanced (Figure 2c: dashed black to dashed red). The addition of a silver mirror, however, causes a significant increase in absorption as light transmitted to the rear surface of glass substrate is reflected, and experiences a double-pass through the ITO (Figure 2c, green curve). Near the CIGSe bandgap, where
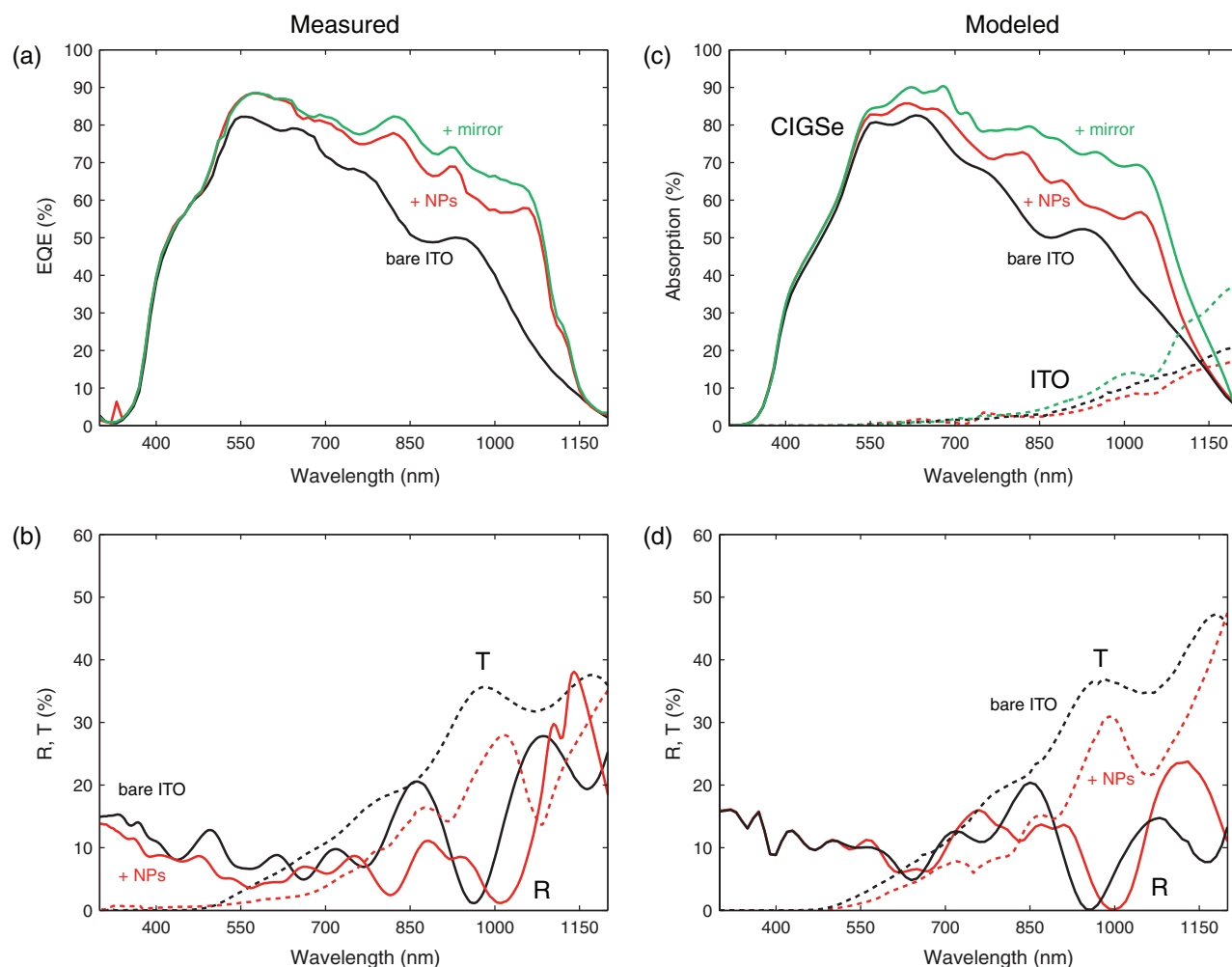
Figure 2. Measured and modeled spectra for ultrathin CIGSe solar cells on ITO. a) Measured EQE curves for cells on bare ITO (black), ITO with SiO$_x$ nanoparticles (red), and with both the nanoparticles and a Ag rear mirror (blue). b) Measured reflection and transmission (solid and dashed lines, respectively) for flat cells on bare ITO (black) and with the nanoparticles (red). c) Simulated absorption within the CIGSe absorber (solid lines), and parasitic absorption within the rear ITO (dashed lines). d) Modeled reflection and transmission for flat (black) and nanopatterned (red) cells.

nearly all light is transmitted, the mirror produces the expected 2× increase in ITO absorption.

Remarkably, in both the measured EQE and the modeled Abs$_{CIGSe}$, a significant enhancement above the flat reference cell is observed from 550 to 1150 nm (Figure 2a,c). This enhancement results from the combined effects of Fabry–Pérot resonances, and efficient coupling into the waveguide modes of the CIGSe absorber layer.
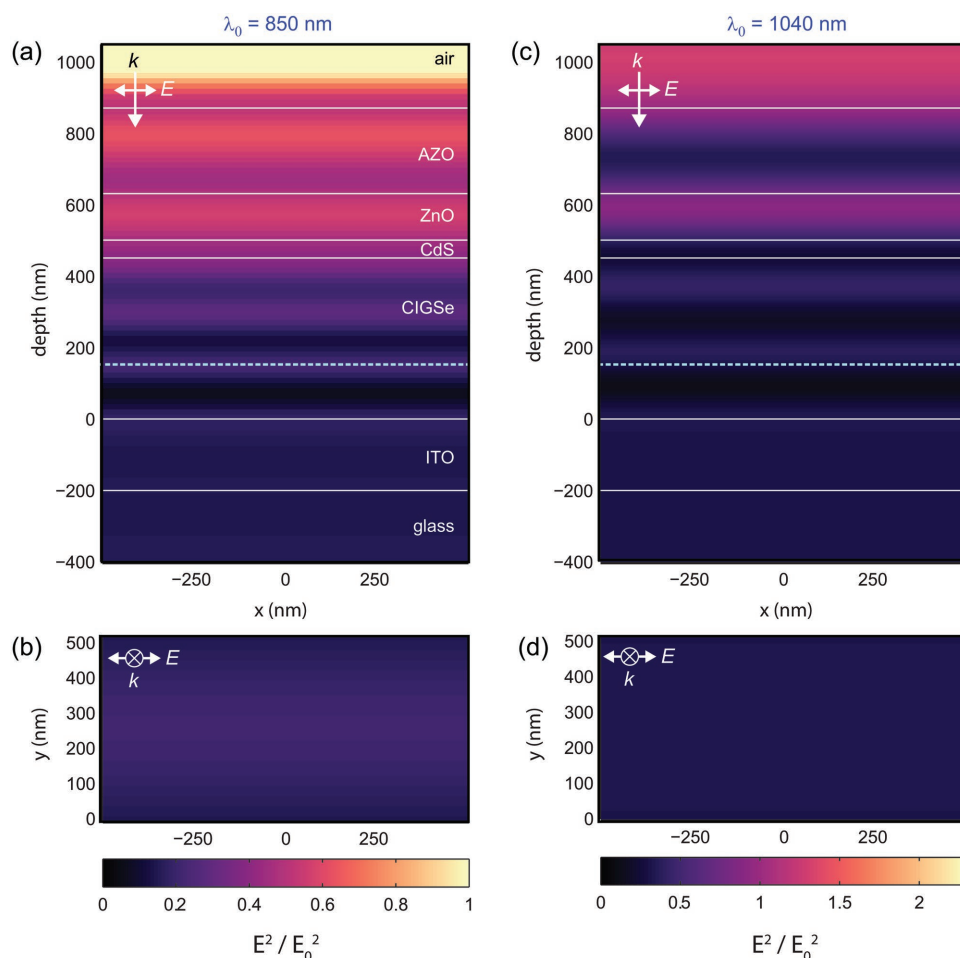
Planar CIGSe solar cells, which are translationally invariant, have an electric field distribution determined entirely by 1D Fabry–Pérot resonances. These resonances account for the oscillations seen in the EQE curve of the planar CIGSe cell (Figure 2, black line), and will adiabatically shift to longer wavelengths as the CIGSe absorber thickness is increased. The calculated field distributions are shown in **Figure 3** for a CIGSe cell with a 452 nm thick absorber, which corresponds to the absorber volume of a 390 nm thick cell with the 513 nm pitched NP inclusions. This allows a straightforward comparison with the nanoparticle-enhanced cell shown in **Figure 4**. The fields are plotted at $\lambda_0 = 850$ and 1040 nm, corresponding to the nanoparticle-enhanced

bands of the measured EQE spectra (Figure 2a). At 850 nm wavelength the CIGSe layer has three maxima in E^2/E_0^2, which corresponds to locally enhanced absorption within the CIGSe layer (Figure 3a). For 1040 nm, there are only two regions of local field (and absorption) enhancement (Figure 3c,d).

These thin-film resonances depend sensitively on the film thickness, as shown in Figure 4a. Increasing the CIGSe thickness from 390 nm (black line) to 452 nm (dashed gray line) boosts the absorber volume, simultaneously increasing the fraction of light absorbed near the band edge and shifting the position of the interference fringes. In the nanoparticle-enhanced cell, nanoparticles replace the excess CIGSe volume such that both thicknesses have an equal total absorber volume. To compare the relative absorption of two cells we can define a relative path length enhancement factor κ_a[33]

$$\kappa_a(\lambda) = \frac{\ln\left(1 - A(\lambda)_{CIGSe,\,modified}\right)}{\ln\left(1 - A(\lambda)_{CIGSe,\,reference}\right)} \tag{1}$$

ADVANCED
SCIENCE NEWS
www.advancedsciencenews.com

ADVANCED
OPTICAL
MATERIALS
www.advopticalmat.de

Figure 3. Modeled electric fields for a planar CIGSe cell at $\lambda_0 = 850$ and 1040 nm. The CIGSe layer thickness was set to 452 nm, corresponding to the absorber volume of a 390 nm thick cell with 513 nm pitched NPs. a,b) Modeled enhancement of E^2/E_0^2 at $\lambda_0 = 850$ nm for vertical and in-plane cross sections. For ease of comparison, the plotted cross sections are the same as in Figure 4, where NPs are incorporated within the CIGSe layer. c,d) Field enhancements at $\lambda_0 = 1040$ nm for vertical and in-plane cross sections. The dashed horizontal lines in (a) and (c) indicate the position of the in-plane cross sections (b) and (d) within the CIGSe layer. Note that optical absorption within the CIGSe layer is proportional to the distribution of E^2/E_0^2.

where $\text{Abs}_{\text{CIGSe,reference}}$ is the wavelength-dependent absorption within the flat 390 nm CIGSe layer, and $\text{Abs}_{\text{CIGSe,modified}}$ is the absorption with the altered absorber layer, either with increased thickness and volume, or with the addition of SiO_2 NPs and unchanged volume. For the planar cells, the κ_a spectrum shows periodic enhancement, corresponding to redshifted Fabry–Pérot resonances (Figure 4b, dashed gray line).

The introduction of nanoparticles within the CIGSe layer yields additional absorption enhancements (Figure 4b). Path length enhancement spectra are shown for three pitches: 513 nm (blue lines, used for the experimental cells), 530 nm (orange), and 550 nm (green). For short wavelengths (<480 nm) the strong CIGSe absorption leads to negligible differences between calculated enhancements. In this range the relative enhancement spectra are dominated by numerical error, and are not plotted. For wavelengths between 480 and 700 nm the enhancements with NPs closely match the enhancement using only the thicker 452 nm CIGSe layer, regardless of pitch. These equivalent enhancements show that Fabry–Pérot resonances are the dominant enhancement mechanism for short wavelengths, and not
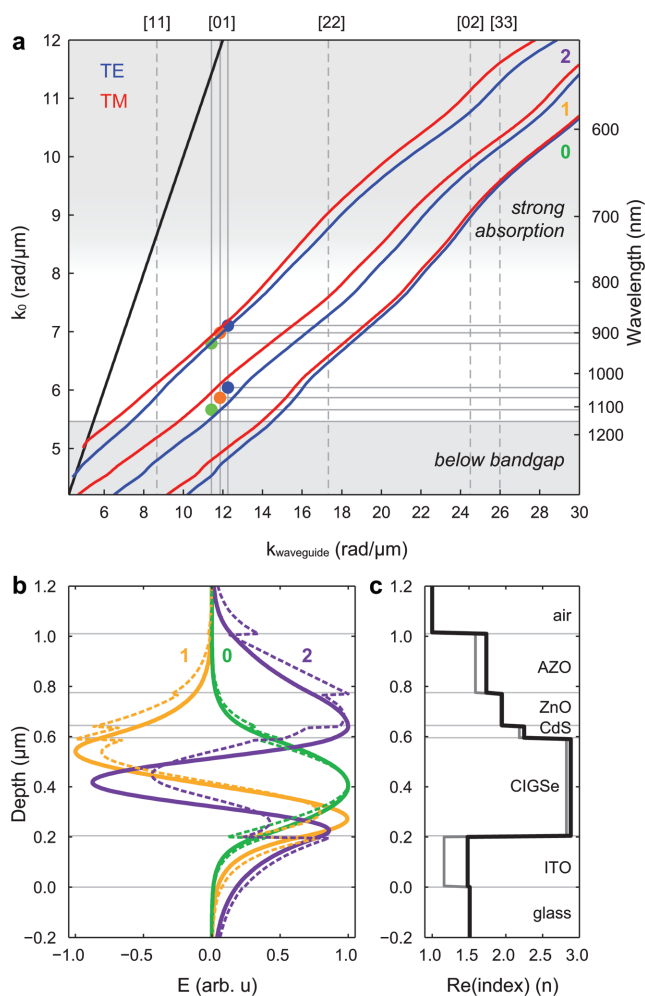
a difference in CIGSe absorber volume. For longer wavelengths the NP-modified cells show significant additional enhancements relative to the thicker absorber (452 nm CIGSe), despite having a lower total CIGSe volume. For the experimental 513 nm pitch, the enhancements peak at 850 and 1040 nm, where NP-related enhancement occurs in addition to the Fabry–Pérot-related field localization. Increasing the nanoparticle pitch from 513 to 530 nm (orange line) and 550 nm (green line) results in a linear shift in these enhancement peaks, suggesting coupling with waveguided modes within the CIGSe layer.[34,35] Simulated electric field distributions at both wavelengths (Figure 4c–f) support this interpretation, showing nanoparticle-induced periodic field enhancements. For the enhancement peak at 1040 nm, which is close to the band edge, the fraction of photons absorbed is significantly improved relative to bare cells (66% vs 44%), which underlines the substantial impact of the nanoparticles on J_{sc} (a gain of 6.4 mA cm^{-2}). Importantly, these field distributions show that the enhanced absorption is localized within the CIGSe layer, rather than the underlying ITO, which supports our observed reduction in parasitic ITO absorption (Figure 2c).

FULL PAPER
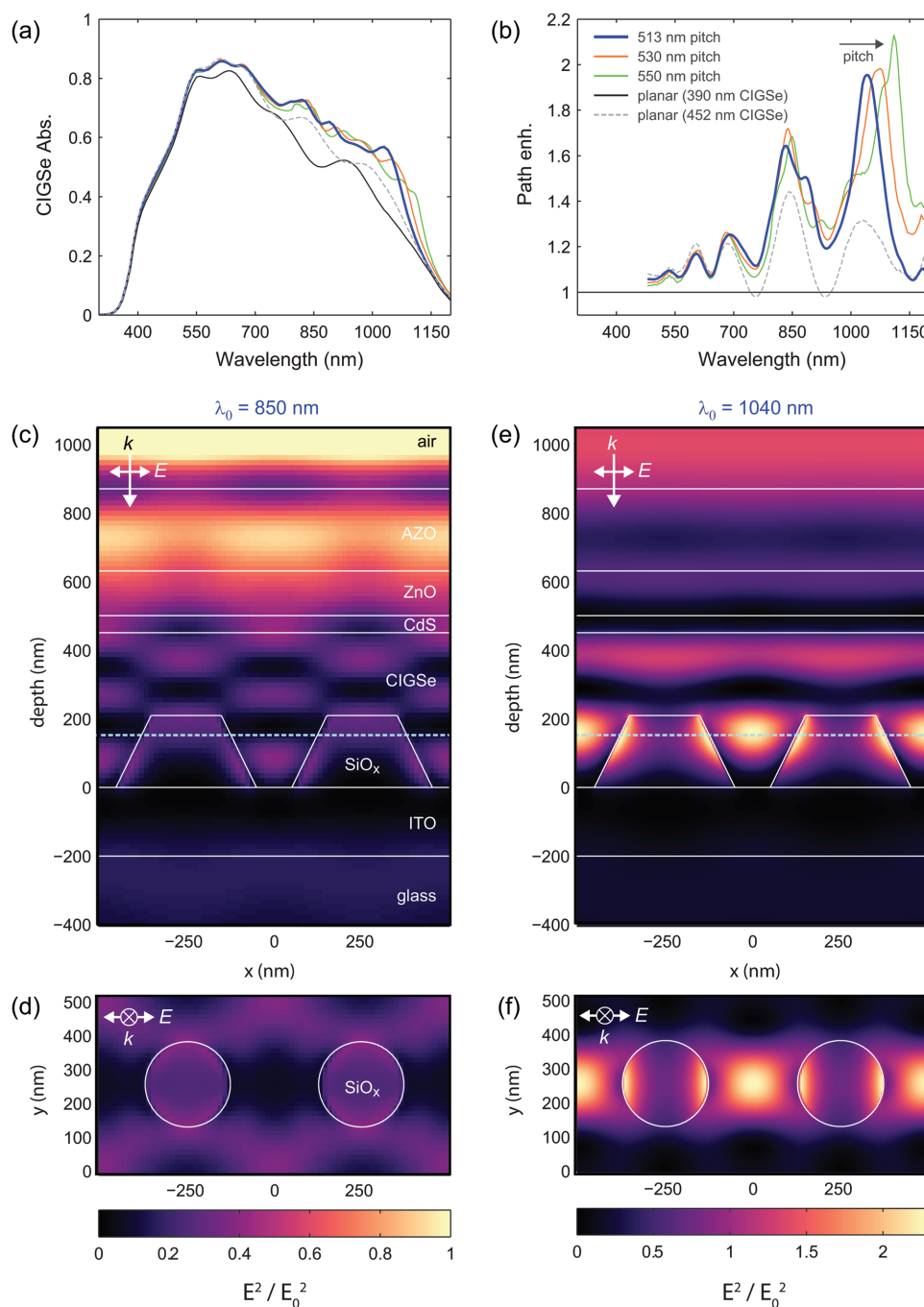
Figure 4. Origin of the EQE enhancement from adding nanoparticles at the CIGSe/ITO interface. a) Modeled CIGSe absorption for three different pitches of NPs: 513 (corresponding to the experimental measurements), 530, and 550 nm. The CIGSe layer thickness was 452 nm for all three pitches, corresponding to the absorber volume of a 390 nm planar layer, and was held constant to avoid shifting the Fabry–Pérot resonance frequencies. The absorption for planar cells with absorber layers of 390 and 452 nm are shown for comparison. b) Absorption enhancement for each model geometry, according to Equation (1), referenced to the 390 nm thick planar CIGSe cell. The legend indicates pitch for cells with NPs, and CIGSe layer thickness for the two planar reference cells. c,d) Modeled enhancement of E^2/E_0^2 at $\lambda_0 = 850$ nm for vertical and in-plane cross sections of a NP-enhanced cell with a 513 nm pitch. e,f) Field enhancements at $\lambda_0 = 1040$ nm for vertical and in-plane cross sections. The dashed horizontal lines in (c) and (e) indicate the position of the in-plane cross sections (d) and (f).

To fully elucidate the nature of the waveguiding enhancements, the dispersion relations for the lowest-order waveguide modes of the planar 390 nm thick CIGSe cell are shown in **Figure 5**a. The modal calculations took into account the full layer structure of the cell using the same measured dielectric functions as in the FDTD modeling (see the Experimental Section: Mode-Solver). Similar modal calculations were previously reported for a-Si:H cells.[36] Due to its high refractive index

ADVANCED
SCIENCE NEWS
www.advancedsciencenews.com

ADVANCED
OPTICAL
MATERIALS
www.advopticalmat.de

FULL PAPER

Figure 5. Fundamental waveguide modes. a) Dispersion relations for the TE (blue) and TM (red) waveguide modes in the 390 nm CIGSe layer. The solid black line is the light line in air. Grating orders for the experimental 513 nm array pitch are indicated by the vertical dashed lines; solid vertical lines correspond to the [01] order of the modeled pitches of 513, 530, and 550 nm. The enhancement peaks from Figure 4b are plotted as the colored points (blue – 513 nm, orange – 530 nm, green – 550 nm), with horizontal lines for ease of identifying the corresponding wavelengths. Enhanced absorption is required between ≈800 and 1150 nm; the shaded regions correspond to spectral regions where CIGSe either already absorbs the light within a single pass, or cannot absorb due to the band gap. b) Mode profiles for the first three TE (solid lines) and TM (dashed lines) modes: TE0/TM0 (green), TE1/TM1 (orange), and TE2/TM2 (purple). For ease of comparison all modes are calculated at $\lambda_0 = 850$ nm. The horizontal gray lines indicate material interfaces. c) Refractive indices of the constituent cell materials at 850 nm (black line) and 1045 nm (gray line).

relative to the other consituent materials ($n_{CIGSe} = 3.2$–2.8 in the 350–1200 nm spectral range), the CIGSe absorber layer forms an optical waveguide. In the wavelength range where CIGSe absorbs weakly ($\lambda_0 \approx 800$–1150 nm), the layer structure supports only three transverse electric (TE) and three transverse magnetic (TM) modes. These modes are located to the right of the light line, which both prevents light within these modes from leaking out of the CIGSe cell and prevents coupling of solar photons into the modes. To enable excitation

of these modes, and thereby increase the optical path length inside the cell, additional in-plane momentum is required. This momentum compensation is provided by the SiO_2 NP lattice, where the CIGSe waveguide modes intersect the grating lines, light can couple into these modes (Figure 5a). In practice, the absorption enhancement corresponding to each mode occurs over a broad spectral range, with the bandwidth determined by absorption and a corresponding uncertainty in the wavevector.

The pitch-dependent absorption enhancements modeled for the full 3D cell geometry agree closely with the dispersion curves plotted in Figure 5a. The nanoparticle-dependent enhancement peaks plotted in Figure 4b, which tune with pitch, are plotted for the [01] grating order (circles). For all three pitches (513, 530, and 550 nm) these agree closely with the calculated TE1 and TE2 dispersion relations, indicating that the SiO_2 nanoparticles only weakly perturb the waveguide modes of the CIGSe layer.

The modal electric field distributions for the TE and TM modes are shown in Figure 5b, along with the corresponding refractive indices (Figure 5c). For the TE1 mode (solid orange), which corresponds to the dominant EQE enhancement around 1040 nm (Figure 5a), the electric field distribution shows two clear maxima in the CIGSe layer. This agrees with the field distribution calculated using the full 3D FDTD model (Figure 4e,f), where the enhancements are entirely aligned with the driving electric field. The 3D modeled fields in the cell do not show discontinuities, indicating a weak TM contribution with enhancements dominated by the TE waveguide mode. The higher energy TE2 mode (solid purple) has three field maxima within the CIGSe layer. The 3D simulated electric field distribution is more complex at this higher energy (Figure 4c,d), which could result from coupling with both the [01] and [22] grating orders. The lowest order modes (TE0/TM0), while offering excellent confinement within the CIGSe layer, lie below the CIGSe bandgap for the [01] grating order and do not contribute significantly to the EQE enhancement.

2.3. Cell Performance Parameters

The experimental current density–voltage (*J*–*V*) parameters for the planar and nanoparticle-enhanced cells are averaged from five cells individually and summarized in **Table 1**. The corresponding *J*–*V* curves are shown in the Supporting Information. The active area J_{sc} values derived from integrating the measured EQE are included and are consistent with the total area values determined directly from *J*–*V* measurements. J_{sc} is increased from 25.5 mA cm^{-2} (bare cells) to 32.4 mA cm^{-2} via the addition of the SiO_x nanoparticles and a Ag mirror. At the same time, the V_{oc} increases from 518 to 558 mV and FF from 50.7% to 55.2%. Overall, the efficiency value is significantly improved from 6.8% to 10.0%.

Using a simple one-diode equation,[37] the expected gain in V_{oc} due to the increased J_{sc} can be estimated as follows

$$V_{oc} = \frac{E_a}{q} - \frac{AkT}{q} \ln\left(\frac{J_{00}}{Jsc}\right) \qquad (2)$$

**ADVANCED
OPTICAL
MATERIALS**
www.advopticalmat.de

**ADVANCED
SCIENCE NEWS**
www.advancedsciencenews.com

FULL PAPER

Table 1. J–V parameters of ultrathin CIGSe solar cells on ITO back contact averaged from five solar cells.

	V_{oc} [mV]	J_{sc} [mA cm^{-2}]	Integrated EQE [mA cm^{-2}]	FF [%]	Efficiency [%]
Cell	518 ± 5	25.5 ± 0.3	25.7	50.7 ± 1.3	6.8 ± 0.1
Cell + NPs	533 ± 3	30.5 ± 0.2	30.9	53.9 ± 2.0	8.8 ± 0.4
Cell + NPs + mirror	558 ± 2	32.4 ± 0.2	32.1	55.2 ± 1.7	10.0 ± 0.3

where k is the Boltzmann constant, q is the electron charge, A is the diode ideality factor, E_a is the activation energy of the dominant recombination mechanism (which is typically equal to E_g), and J_{sc} and J_{00} represent the photogenerated current density and saturation current density prefactor, respectively. Assuming that the J_{sc} increase is the only reason for the V_{oc} improvement, the expected V_{oc} increase is 11.6 mV from bare cells to cells with SiO$_x$ nanoparticles and 14.6 mV from bare cells to cells with both SiO$_x$ nanoparticles and Ag mirror. Room temperature is assumed and A is set to 2.0 which is the maximum value for thermally activated recombination. However, the experimental increase in V_{oc} is significantly larger than the calculated value (40 mV measured improvement), pointing to an additional recombination mechanism in our ultrathin CIGSe solar cells.

To better understand the cause of this anomalous V_{oc} increase, temperature dependent current density–voltage (J–V(T)) measurements were performed for bare cells and the cells with SiO$_x$ nanoparticles and Ag back reflector in the temperature range from 180 to 320 K under an illumination density of 0.85 sun (**Figure 6**). Representative J–V curves are plotted at temperatures of 200, 250, and 300 K in Figure 6a,b. Bare cells on ITO exhibited a reduced slope in the forward current region as the temperature was reduced, leading to nonideal J–V curves. This effect is likely due to a back barrier (Φ_b) at the CIGSe/ITO interface,[38,39] which could induce a reversed space charge region (in addition to the main CdS/CIGSe junction). This would explain the nonideal J–V curves, which are typical for TCO-based CIGSe cells,[24,39] and presents a significant contrast to typical Mo-based cells where the back barrier potential Φ_b is negligible due to the existence of MoSe$_2$ at the back interface.[40,41] Remarkably, this nonideality is less pronounced for cells with the SiO$_x$ nanoparticles and Ag mirror, indicating that Φ_b is reduced compared to the bare cell. The influence of Φ_b on V_{oc} can be especially pronounced in ultrathin CIGSe solar cells where the primary space charge region is close to, or overlaps with, the inverse space charge region extending from the back contact.[42] Figure 6c shows V_{oc} as a function of temperature. According to Equation (2), E_a can be determined by extrapolating $V_{oc}(T)$ curves from the high temperature linear regime to $T = 0$ K. When the back barrier is not negligible, E_a in Equation (2) should be adapted to $E_g - \Phi_b$.[42] E_a is extrapolated to be around 800 meV for bare cells and is much higher (1050 meV) for cells with SiO$_x$ nanoparticles and a Ag mirror. This again indicates a smaller barrier Φ_b in cells with light trapping schemes. It is not completely clear why the back barrier is reduced by adding the SiO$_x$ nanoparticles and Ag mirror, although we speculate that the locally increased density of photogenerated carriers modifies the trapped charge density near the back contact, producing a photoinduced band bending near the back contact.[43] The

existence of a back barrier increases the series resistance and thus reduces the FF.[44] Since the nanopatterned cells exhibit a lower Φ_b, the FF improves from 50.7% to 55.2%.
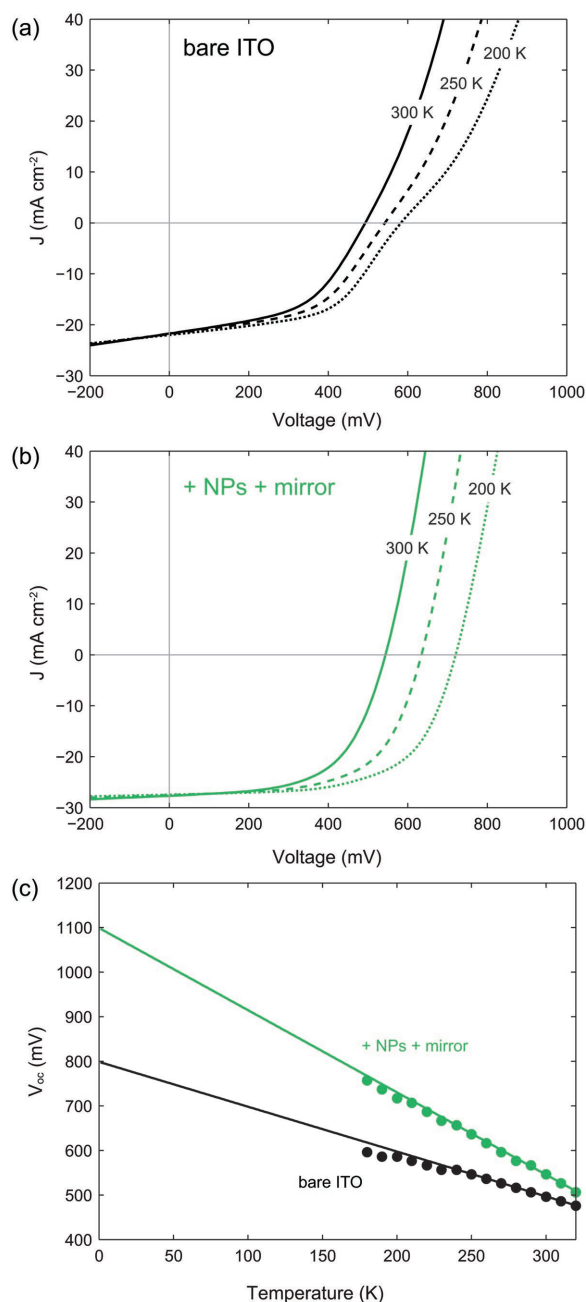
2.4. EQE Comparison with the World Record Cell and Further Opportunities

Highly efficient thick CIGSe solar cells with a MgF$_2$ antireflection layer typically have a J_{sc} value of ≈36 mA cm^{-2} with a [Ga]/([Ga]+[In]) ratio of 0.3–0.35.[45] To understand the remaining optical losses after adding the SiO$_x$ nanoparticles and mirror, we compare the EQE curves of our solar cells (CIGSe thickness $d_{CIGSe} = 390$ nm, [Ga]/([Ga]+[In]) = 0.36) to the thick solar cells with a world record efficiency value of 21.7% ($d_{CIGSe} = 2.5$–3.0 μm, [Ga]/([Ga]+[In]) = 0.32) in **Figure 7**. The record efficiency value is currently 22.6%[1] but, since the parameters for this cell are not yet available, we compare our EQE to the previous record cell with an efficiency value of 21.7%.[45]

To be comparable, we first coated an antireflection layer of closely packed 120 nm diameter silica spheres (similar to the typical MgF$_2$).[46] The resulting sample is presented as an inset in Figure 7, which shows eight individual ultrathin solar cells on the 2.5 × 2.5 cm^2 substrate. The shiny surface is due to the periodically nanostructured surface arising from conformal growth over the SiO$_x$ nanoparticles. The EQE curve for an antireflection-coated cell with nanoparticles and a rear Ag mirror is plotted in violet in Figure 7. The integrated J_{sc} for this cell reaches 34.0 mA cm^{-2}, which is 93% of the J_{sc} value from the record cell, demonstrating that ultrathin CIGSe solar cells with an absorber thickness of 390 nm can exhibit a comparable absorption to their thick counterparts. To our knowledge, this is the highest J_{sc} value yet achieved for an ultrathin CIGSe solar cell.
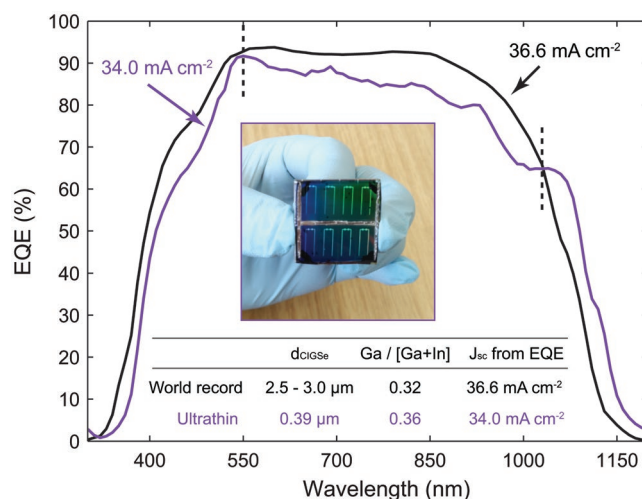
To study the EQE comparison in more detail, we split the whole spectrum of interest into three subranges. In the short wavelength range (300–530 nm), light can be completely absorbed before reaching the back contact in thick CIGSe solar cells as well as in our ultrathin ones. The superior EQE performance of the reference thick solar cells in this range accounts for 0.8 mA cm^{-2} in J_{sc}. This is attributed to the potassium fluoride-induced thinning of CdS and thus reduced parasitic absorption in CdS,[47] which was not applied in our ultrathin CIGSe solar cells. Beyond 1030 nm, the ultrathin CIGSe solar cells perform even better, corresponding to a J_{sc} difference of 0.70 mA cm^{-2}. This long-wavelength enhancement is primarily due to the waveguided modes populated by the nanophotonic back contact, as shown in Figures 4 and 5. A minor contribution may also result from slight differences between the minimum absorber bandgap in the two cells. In the range of 530–1030 nm,

**ADVANCED
SCIENCE NEWS**

www.advancedsciencenews.com

**ADVANCED
OPTICAL
MATERIALS**

www.advopticalmat.de

FULL PAPER

Figure 7. Comparison of EQE curves between our ultrathin CIGSe solar cells (violet) and world record thick solar cells (black). The inset table gives the related solar cell parameters, the image is the photograph of the ultrathin CIGSe solar cells on 2.5 × 2.5 cm^2 substrate with shiny surface, due to the periodic surface nanostructure originating from conformal growth on SiO$_x$ nanoparticles.

Figure 6. J–V curves of a) bare cells (black) and b) cells with SiO$_x$ nanoparticles and Ag mirror (green) under illumination measured at temperatures of 200 K (dotted line), 250 K (dashed line), and 300 K (solid line). (c) Temperature dependent open-circuited voltage V_{oc} (T) for bare cells (black points) and cells with SiO$_x$ nanoparticles and Ag mirror (green points), V_{oc} (T = 0 K) is extrapolated (solid lines) to yield the activation energy of the dominant recombination mechanism.

the ultrathin solar cells are modestly less efficient relative to thick cells, with Abs$_{ITO}$ largely responsible (see Figure 2b); this loss may be mitigated in future designs by optimizing the geometry of the SiO$_x$ nanoparticles or by substituting ITO with a less lossy TCO. Moreover, our ultrathin CIGSe solar cells have a slightly higher [Ga]/([Ga]+[In]) ratio (0.36) than the reference cell (0.32), indicating that the absorption coefficient is

overall larger for the world record solar than for our ultrathin ones. This means that the absorption difference can be further reduced if ultrathin cells have the same [Ga]/([Ga]+[In]) ratio of 0.32. Considering all the optimization opportunities mentioned above, it is quite likely that a J_{sc} value beyond 35 mA cm^{-2} is achievable for ultrathin CIGSe solar cells.

Since the preparation process for our ultrathin solar cells is not yet fully optimized (e.g., potassium fluoride (KF) treatment, [Ga]/([Ga]+[In]) profile), these cells are not yet comparable to record CIGSe cells in V_{oc} and FF (see Supporting Information for detailed comparison). Even compared to reported ultrathin solar cells prepared on Mo,[10,13,48] the ITO-based cells are still electrically inferior in terms of lower V_{oc} and FF. The main reason for this electrical deficit is the continued influence of the barrier at the ITO/CIGSe interface which is not completely eliminated by the nanophotonic contact. To reach the record-class performance demonstrated by Mo-based cells, the barrier at the back contact must be further reduced. In ref. [39] it was demonstrated that a few-nm thick hole transporting layer (MoO$_3$) was able to eliminate the potential barrier, enabling comparable electrical properties between cells on TCO and Mo. This points to a promising path toward highly efficient ultrathin CIGSe solar cells on TCO substrates.

3. Conclusion

In conclusion, we have experimentally integrated SiO$_x$ nanoparticles at the rear interface of ultrathin CIGSe solar cells on ITO with an absorber thickness of 390 nm and a [Ga]/([Ga]+[In]) ratio of 0.36. SiO$_x$ nanoparticle arrays give rise to significant light trapping effects in the long wavelength range and overall contribute to a remarkable increase of 5.0 mA cm^{-2} in J_{sc}. FDTD and eigenmode modeling showed that these effects were due to the creation of Fabry–Pérot and waveguided resonances

**ADVANCED
OPTICAL
MATERIALS**

www.advopticalmat.de

**ADVANCED
SCIENCE NEWS**

www.advancedsciencenews.com

FULL PAPER

emerging from the incorporation of SiO_x nanoparticles beneath a conformal CIGSe layer. It was also shown that absorption enhancement near the back interface electrically benefits CIGSe solar cells by reducing the back barrier for cells on ITO. Consequently, the efficiency value significantly increases from 6.8% for flat cells on ITO to 10.0% for cells with both SiO_x nanoparticles and a Ag mirror. With the addition of an antireflection layer, the J_{sc} of these nanopatterned ultrathin CIGSe solar cells reached 34.0 mA cm^{-2}. This is the highest experimental J_{sc} yet reported for any ultrathin CIGSe solar cell and accounts for 93% of the J_{sc} value of a record thick solar cell, indicating that the challenge of attaining high optical absorption within ultrathin CIGSe solar cells has been addressed. Combined with further improvements in electrical quality, this provides a path toward ultrathin CIGSe solar cells with efficiency values exceeding 20%.

4. Experimental Section

Fabrication of SiO$_x$ Nanoparticles on ITO Substrates: Substrate conformal imprint lithography (SCIL) was used to prepare SiO_x nanoparticle arrays on ITO-coated glass substrates. The substrates were first spin-coated with a bilayer of polymethyl methacrylate (PMMA, 550 nm) and silica sol–gel (70 nm). A PDMS stamp containing the desired nanopattern was then applied to the liquid sol–gel layer for 20 min, allowing the solvents to evaporate and—following stamp release—leaving behind a patterned layer of ≈90 wt% silica, with a small residual fraction of organics. The pattern was then transferred from this hard mask into the PMMA using an O_2 plasma etch, which was timed to create an undercut, followed by electron-beam evaporation of SiO_2 and lift-off in acetone. The tapered geometry of the SiO_x nanoparticles was the result of self-shadowing as silica built up on the edges of the sacrificial sol–gel/PMMA mask during the evaporation, producing a progressive narrowing of the effective mask diameter.

FDTD Modeling: Simulations were performed using a commercial grade FDTD solver.[49] The simulation region was uniformly discretized using square $5 \times 5 \times 5$ nm^3 elements; this mesh size was chosen after convergence testing to minimize computational requirements while maintaining accuracy. Perfectly matched layers were used at the top and bottom of the simulation volume, with antisymmetric/symmetric boundaries in x and y dimensions, respectively, to achieve a 4× reduction in the simulated volume.

Mode-Solver: Maxwell's equations were solved, subject to continuity of the tangential electric and magnetic fields within the cell layers, to find the fundamental TE and TM waveguided modes.[50] The solution was performed for both TE and TM modes using a custom mode-solver, which enabled the calculation of both the dispersion relation and electric field profile for each mode. Only purely bound waveguided modes were considered, where the modal field decays to zero far away from the waveguide. The calculated layer structure was the same as shown in Figure 1c, where measured dielectric functions were used for all layers.

Preparation Details of CIGSe Solar Cells: The back contact was a 200 nm layer of ITO with a sheet resistance of <10 Ω sq^{-1}. The CIGSe absorber was evaporated by the so-called three-stage process at a substrate temperature of 450 °C where the low substrate temperature facilitates the formation of a steep back Ga grading that reduces back recombination.[10] X-ray fluorescence shows the CIGSe thickness of 390 nm and [Ga]/([Ga]+[In]) = 0.36, [Cu]/([Ga]+[In]) = 0.87. A 50 nm CdS buffer layer was formed via chemical bath deposition.[51] Next, a sputtered 130 nm intrinsic ZnO and a 240 nm AZO (Al:ZnO) layer followed. Finally, the Ni/Al front contact was e-beam evaporated through a shadow mask. For electrical measurements, the solar cells were mechanically scribed to an active cell area of 0.5 cm^2. Each layer deposition and cell performance characterizations were done simultaneously on all cells described in this work.

Supporting Information

Supporting Information is available from the Wiley Online Library or from the author.

[1] ZSW, "ZSW Sets New World Record for Thin-film Solar Cells". https://www.zsw-bw.de/en/newsroom/news/news-detail/news/detail/News/zsw-sets-new-world-record-for-thin-film-solar-cells.html (accessed: June 2016).

[2] PV Magazine, "Inside TSMC's 16.5% CIGSe module world record". http://www.pv-magazine.com/news/details/beitrag/inside-tsmcs-165-cigs-module-world-record_100019430/#axzz41ptOE2Qd (accessed: May 2015).

[3] CIGSe community, "White paper for CIGSe thin film solar cell technology". http://cigs-pv.net/ (accessed: September 2016).

[4] A. Polman, M. Knight, E. C. Garnett, B. Ehrler, W. C. Sinke, *Science* **2016**, *352*, aad4244.

[5] V. Fthenakis, *Renewable Sustainable Energy Rev.* **2009**, *13*, 2746.

[6] C. S. Tao, J. Jiang, M. Tao, *Sol. Energy Mater. Sol. Cells* **2011**, *95*, 3176.

[7] N. Dahan, Z. Jehl, T. Hildebrandt, J.-J. Greffet, J.-F. Guillemoles, D. Lincot, N. Naghavi, *J. Appl. Phys.* **2012**, *112*, 094902.

[8] M. Gloeckler, J. R. Sites, *J. Appl. Phys.* **2005**, *98*, 103703.

[9] O. Lundberg, M. Bodegård, J. Malmström, L. Stolt, *Prog. Photovoltaics Res. Appl.* **2003**, *11*, 77.

[10] G. Yin, V. Brackmann, V. Hoffmann, M. Schmid, *Sol. Energy Mater. Sol. Cells* **2014**, *132*, 142.

[11] B. Vermang, V. Fjällström, J. Pettersson, P. Salomé, M. Edoff, *Sol. Energy Mater. Sol. Cells* **2013**, *117*, 505.

[12] F. Erfurth, Z. Jehl, M. Bouttemy, N. Dahan, P. Tran-Van, I. Gerard, A. Etcheberry, J.-J. Greffet, M. Powalla, G. Voorwinden, D. Lincot, J. F. Guillemoles, N. Naghavi, *Appl. Surf. Sci.* **2012**, *258*, 3058.

[13] Z. J. Li-kao, N. Naghavi, F. Erfurth, J. F. Guillemoles, I. Gérard, A. Etcheberry, J.L. Pelouard, S. Collin, G. Voorwinden, D. Lincot, *Prog. Photovoltaics Res. Appl.* **2012**, *20*, 582.

[14] H. A. Atwater, A. Polman, *Nat. Mater.* **2010**, *9*, 205.

[15] P. Spinelli, V. E. Ferry, C. van Lare, J. van de Groep, M. A. Verschuuren, R. E. I. Schropp, H. A. Atwater, A. Polman, *J. Opt.* **2012**, *14*, 24002.

**ADVANCED
SCIENCE NEWS**

www.advancedsciencenews.com

**ADVANCED
OPTICAL
MATERIALS**

www.advopticalmat.de

FULL PAPER

[16] V. E. Ferry, A. Polman, H. A. Atwater, *ACS Nano* **2011**, *5*, 10055.

[17] M. Schmid, P. Andrae, P. Manley, *Nanoscale Res. Lett.* **2014**, *9*, 50.

[18] G. Yin, A. Steigert, P. Andrae, M. Goebelt, M. Latzel, P. Manley, I. Lauermann, S. Christiansen, M. Schmid, *Appl. Surf. Sci.* **2015**, *355*, 800.

[19] M. Schmid, P. Andrae, P. Manley, *Nanoscale Res. Lett.* **2014**, *9*, 50.

[20] P. Spinelli, M. A. Verschuuren, A. Polman, *Nat. Commun.* **2012**, *3*, 692.

[21] M. L. Brongersma, Y. Cui, S. Fan, *Nat. Mater.* **2014**, *13*, 451.

[22] B. Hoex, J. Schmidt, R. Bock, P. P. Altermatt, M. C. M. van de Sanden, W. M. M. Kessels, *Appl. Phys. Lett.* **2007**, *91*, 112107.

[23] C. Van Lare, G. Yin, A. Polman, M. Schmid, *ACS Nano* **2015**, *9*, 9603.

[24] H. Simchi, J. Larsen, K. Kim, W. Shafarman, *IEEE J. Photovoltaics* **2014**, *4*, 6.

[25] T. Nakada, Y. Hirabayashi, T. Tokado, D. Ohmori, T. Mise, *Sol. Energy* **2004**, *77*, 739.

[26] C. Onwudinanti, R. Vismara, O. Isabella, L. Grenet, F. Emieux, M. Zeman, *Opt. Exp.* **2016**, *24*, A693.

[27] D. L. Young, J. Abushama, R. Noufi, X. Li, J. Keane, T. A. Gessert, J. S. Ward, M. Contreras, T. J. Coutts, presented at *the 29th IEEE Photovoltaic Specialist Conf.*, New Orleans, LA, May **2002**.

[28] M. A. Verschuuren, *Ph.D. Thesis*, Utrecht University, **2010**.

[29] M. A. Verschuuren, P. Gerlach, H. A. van Sprang, A. Polman, *Nanotechnology* **2011**, *22*, 505201.

[30] G. Yin, C. Merschjann, M. Schmid, *J. Appl. Phys.* **2013**, *113*, 213510.

[31] E. D. Palik, *Handbook of Optical Constants of Solids*, Elsevier, Germany **1991**.

[32] O. Berger, D. Inns, A. G. Aberle, *Sol. Energy Mater. Sol. Cells* **2007**, *91*, 1215.

[33] U. Ulbrich, M. Peters, B. Bläsi, T. Kirchartz, A. Gerber, U. Rau, *Opt. Exp.* **2010**, *18*, A133.

[34] U. W. Paetzold, S. Lehnen, K. Bittkau, U. Rau, R. Carius, *Nano Lett.* **2014**, *14*, 6599.

[35] S. Mokkapati, K. R. Catchpole, *J. Appl. Phys.* **2012**, *112*, 101101.

[36] M. van Lare, F. Lenzmann, M. A. Verschuuren, A. Polman, *Appl. Phys. Lett.* **2012**, *101*, 221110.

[37] S. S. Hegedus, W. N. Shafarman, *Prog. Photovoltaics Res. Appl.* **2004**, *12*, 155.

[38] G. T. Koishiyev, J. R. Sites, S. S. Kulkarni, N. G. Dhere, presented at *the 33th IEEE Photovoltaic Specialist Conf.*, San Diego, CA, USA, May **2008**.

[39] H. Simchi, B. E. McCandless, T. Meng, W. N. Shafarman, *J. Appl. Phys.* **2014**, *115*, 033514.

[40] K.-J. Hsiao, J.-D. Liu, H.-H. Hsieh, T.-S. Jiang, *Phys. Chem. Chem. Phys.* **2013**, *15*, 18174.

[41] N. Kohara, S. Nishiwaki, Y. Hashimoto, T. Negami, T. Wada, *Sol. Energy Mater. Sol. Cells* **2001**, *67*, 209.

[42] T. Ott, F. Schönberger, T. Walter, D. Hariskos, O. Kiowski, O. Salomon, R. Schäffler, *Thin Solid Films* **2015**, *582*, 392.

[43] T. Eisenbarth, R. Caballero, M. Nichterwitz, C. A. Kaufmann, H. W. Schock, T. Unold, *J. Appl. Phys.* **2011**, *110*, 094506.

[44] Q. Cao, O. Gunawan, M. Copel, K. B. Reuter, S. J. Chey, V. R. Deline, D. B. Mitzi, *Adv. Energy Mater.* **2011**, *1*, 845.

[45] P. Jackson, D. Hariskos, R. Wuerz, O. Kiowski, A. Bauer, T. M. Friedlmeier, M. Powalla, *Phys. Status Solidi RRL* **2015**, *9*, 28.

[46] G. Yin, P. Manley, M. Schmid, *Sol. Energy Mater. Sol. Cells* **2016**, *153*, 124.

[47] A. Chirilă, P. Reinhard, F. Pianezzi, P. Bloesch, A. R. Uhl, C. Fella, L. Kranz, D. Keller, C. Gretener, H. Hagendorfer, D. Jaeger, R. Erni, S. Nishiwaki, S. Buecheler, A. N. Tiwari, *Nat. Mater.* **2013**, *12*, 1107.

[48] B. Vermang, J. T. Watjen, C. Frisk, V. Fjallstrom, F. Rostvall, M. Edoff, P. Salome, J. Borme, N. Nicoara, S. Sadewasser, *IEEE J. Photovoltaics* **2014**, *4*, 1644.

[49] Lumerical Solutions, Inc., http://www.lumerical.com/tcad-products/fdtd/.

[50] E. Verhagen, *Ph.D. Thesis*, Utrecht University, **2009**.

[51] D. Braunger, T. Durr, D. Hariskos, Ch. Koble, T. Walter, N. Wieser, H. W. Schock, *Proc. 25th IEEE Photovoltaic Specialist Conf.*, IEEE, Washington DC, USA **1996**.